Doppler Exploitation in Bistatic mmWave Radio SLAM

Citation for the original published paper (version of record):
Ge, Y., Kaltiokallio, O., Chen, H. et al (2022). Doppler Exploitation in Bistatic mmWave Radio SLAM. GLOBECOM - IEEE Global Telecommunications Conference: 6463-6468.
http://dx.doi.org/10.1109/GLOBECOM48099.2022.10001597

Doppler Exploitation in Bistatic mmWave Radio SLAM

Yu Ge*, Ossi Kaltiokallio†, Hui Chen*, Fan Jiang*, Jukka Talvitie†,
Mikko Valkama†, Lennart Svensson*, Henk Wymeersch*
*Department of Electrical Engineering, Chalmers University of Technology, Gothenburg, Sweden,
†Unit of Electrical Engineering, Tampere University, Tampere, Finland,
{yuge, hui.chen, fan.jiang, lennart.svensson, henkw}@chalmers.se, {ossi.kaltiokallio, jukka.talvitie, mikko.valkama}@tuni.fi

***Abstract*—Networks in 5G and beyond utilize millimeter wave (mmWave) radio signals, large bandwidths, and large antenna arrays, which bring opportunities in jointly localizing the user equipment and mapping the propagation environment, termed as simultaneous localization and mapping (SLAM). Existing approaches mainly rely on delays and angles, and ignore the Doppler, although it contains geometric information. In this paper, we study the benefits of exploiting Doppler in SLAM through deriving the posterior Cramér-Rao bounds (PCRBs) and formulating the extended Kalman-Poisson multi-Bernoulli sequential filtering solution with Doppler as one of the involved measurements. Both theoretical PCRB analysis and simulation results demonstrate the efficacy of utilizing Doppler.**

***Index Terms*—MmWave radio SLAM, Doppler, PCRB, extended Kalman-Poisson multi-Bernoulli filter.**

I. INTRODUCTION

MmWave communications in 5G and beyond are useful for simultaneous localization and mapping (SLAM) applications, due to geometrical propagation channels, large bandwidths, and large antenna arrays [1]. Signals sent from the base station (BS) reach the user equipment (UE) via the propagation channel, which is determined by the geometric relationships among the propagation environment, the UE, and the BS. Large bandwidths and antenna arrays result in high temporal and spatial resolutions [2], [3]. Therefore, state-of-the-art channel estimators can provide accurate estimates for multipath components by using the received signals, in terms of groups of channel gain, time of arrival (TOA), angles of arrival (AOA), angles of departure (AOD), and Doppler, which contain the necessary information for SLAM [4]. Although Doppler contains geometric information, it is usually ignored.

The related works can be divided into two areas: works that exploit Doppler for radio positioning or mapping and works in the area of radio SLAM. Doppler has been used in most radars for mapping and tracking [5], but limited works have been done in radio scenarios. Doppler is used to localize radio emitters in [6], but the proposed method can only be used for narrow-band signals, while [7] shows that the Doppler shift can provide more direction information for localization, and [8] shows that the mobility can significantly improve the non-line-of-sight (NLOS)-only scenario in MIMO mmWave system, indicating the involvement of the Doppler shift brings gain in the localization accuracy. Doppler is used for tracking UEs' positions and velocities in a Wi-Fi-based system in [9]. However, these methods do not solve the SLAM problem. Several approaches have been proposed to address the mmWave radio SLAM problem, including geometry-based methods [10], [11], message passing-based methods [12], [13], and random finite set (RFS)-based methods [14]–[16]. RFS-based methods can handle uncertainties, as well as inherently deal with challenges of the unknown number of landmarks, unknown data associations (DAs), misdetections, and clutter measurements in radio SLAM. Within these RFS-based methods, the probability hypothesis density (PHD) filter is used in [14], which does not have an explicit enumeration of DAs, and the Poisson multi-Bernoulli mixture (PMBM) filter is used in [15], [16], which enumerates all possible DAs explicitly, thus allowing for improved performance. However, the Doppler is not considered in these works. To our best knowledge, the inclusion of Doppler in radio SLAM has not yet been conducted in the existing literature.

In this paper, we harness the Doppler component in bistatic mmWave radio SLAM and analyze how Doppler benefits the SLAM filter. The main contributions of this paper are summarized as follows: (*i*) we derive the position error bound (PEB), heading error bound (HEB), clock bias error bound (CEB) of the UE and the landmark error bounds (LEBs) of landmarks by computing the posterior Cramér-Rao bound (PCRB) for the system with utilizing Doppler; (*ii*) we analyze the effect of the quality of the Doppler measurement on the bounds of the UE and the average LEB of landmarks; (*iii*) we extend our previous work in [16] by involving the Doppler as a dimension of the measurement in the extended Kalman (EK)-Poisson multi-Bernoulli (PMB) SLAM filter, and validate the benefits of exploiting Doppler in the system through numerical experiments in the mmWave network context.

Notations: Scalars (e.g., x) are denoted in italic, vectors (e.g., $\boldsymbol{x}$) in bold lower-case letters with $\|\boldsymbol{x}\|$ representing its L2-norm, matrices (e.g., $\boldsymbol{X}$) in bold capital letters, sets (e.g., $\mathcal{X}$) in calligraphic with $|\mathcal{X}|$ representing its cardinality. The transpose is denoted by $(\cdot)^{\mathsf{T}}$, the Hermitian transpose is denoted by $(\cdot)^{\mathsf{H}}$, the union of mutually disjoint sets is denoted by $\uplus$, the expectation is denoted by $\mathbb{E}[\cdot]$, $\mathcal{N}(\boldsymbol{u}, \boldsymbol{\Sigma})$ denotes a multivariate Gaussian distribution with mean $\boldsymbol{u}$ and covariance $\boldsymbol{\Sigma}$, and $d_{\boldsymbol{x}} = \dim(\boldsymbol{x})$.

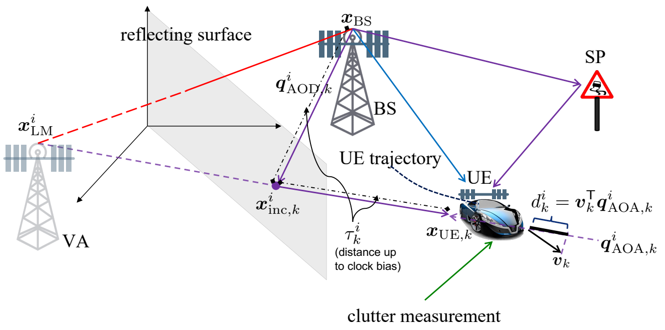

Fig. 1. A mmWave downlink scenario with the environment of a BS, a UE, a reflecting surface, and a small object. The reflecting surface can be modeled as a virtual anchor (VA), which is the reflection of the BS with respect to the surface. The small object is modeled as a scattering point (SP). The BS sends signals to the UE via line-of-sight (LOS) path and/or NLOS paths, shown as the blue line and purple lines, respectively. The channel parameters of each path depend on the underlying geometry.

II. SYSTEM MODEL

In this section, the UE model, the environment model, the signal model, and the measurement model for a mmWave radio downlink scenario as shown in Fig. 1 are briefly introduced.

A. State Models

In this paper, a single-user scenario is considered, where the UE does a constant turn-rate movement around a known BS on the $x-y$ plane. We denote the dynamic state of the UE at time step k as $\boldsymbol{s}_k = [x_k, y_k, \varpi_k, b_k]^{\mathsf{T}}$, containing the UE position on x- and y-axis, heading, and clock bias, respectively. The UE dynamics can be expressed as [17]

$$\underbrace{\begin{bmatrix} x_k \\ y_k \\ \varpi_k \\ b_k \end{bmatrix}}_{\boldsymbol{s}_k} = \underbrace{\begin{bmatrix} x_{k-1} + \frac{2v}{\omega}\sin\left(\frac{\omega T}{2}\right)\cos\left(\varpi_{k-1} + \frac{\omega T}{2}\right) \\ y_{k-1} + \frac{2v}{\omega}\sin\left(\frac{\omega T}{2}\right)\sin\left(\varpi_{k-1} + \frac{\omega T}{2}\right) \\ \varpi_{k-1} + \omega T \\ b_{k-1} \end{bmatrix}}_{\boldsymbol{f}(\boldsymbol{s}_{k-1})} + \boldsymbol{\eta}_k, \tag{1}$$

where v, ω, and T are known control inputs, denoting the speed, the turn-rate, and the sampling interval, respectively, and $\boldsymbol{\eta}_k \sim \mathcal{N}(\boldsymbol{0}, \boldsymbol{Q})$.

The considered scenario contains a single known BS, and multiple unknown reflecting surfaces and small objects, which are modeled as VAs and SPs, respectively. The BS sends downlink signals to the UE, which can reach the UE directly, termed as the LOS path, and/or can be reflected by the reflecting surfaces or scattered by the small objects and reach the UE, termed as NLOS paths (see Fig. 1). In this paper, we assume that there is at most one path associated to each landmark every time step. The landmark state can be modeled as $\boldsymbol{x} = [\boldsymbol{x}_{\text{LM}}^{\mathsf{T}}, m]^{\mathsf{T}}$, with $\boldsymbol{x}_{\text{LM}} \in \mathbb{R}^3$ denoting the landmark location, and $m \in \{\text{BS}, \text{VA}, \text{SP}\}$ denoting the landmark type. Therefore, the map of the environment can be modeled by a set of landmark $\mathcal{X} = \{\boldsymbol{x}^1, \ldots, \boldsymbol{x}^I\}$, with I representing the total number of landmarks.

B. Signal Model

The BS sends downlink signals to the UE at every time step with a period of T seconds. These signals can reach the UE via LOS path and/or NLOS paths, and the received signal for OFDM symbol n, at subcarrier κ and time step k can be expressed as [18]

$$\boldsymbol{y}_{\kappa,n,k} = \boldsymbol{W}_{n,k}^{\mathsf{H}} \sum_{i=1}^{I_k} g_k^i \boldsymbol{a}_{\text{R}}(\boldsymbol{\theta}_k^i) \boldsymbol{a}_{\text{T}}^{\mathsf{H}}(\boldsymbol{\phi}_k^i) e^{-\jmath 2\pi\kappa\Delta f \tau_k^i} \times e^{\jmath 2\pi n T_{\text{mea}} d_k^i/\varsigma} \boldsymbol{p}_{n,k} + \boldsymbol{W}_{n,k}^{\mathsf{H}} \boldsymbol{n}_{\kappa,n,k}, \tag{2}$$

where $\boldsymbol{y}_{\kappa,n,k}$ denotes the received signal, $\boldsymbol{p}_{n,k}$ denotes the pre-coded pilot signal, $\boldsymbol{n}_{\kappa,n,k}$ denotes a white Gaussian noise, $\boldsymbol{W}_{n,k}$ denotes a combining matrix, I_k denotes the number of all visible landmarks at time k, $\boldsymbol{a}_{\text{R}}(\cdot)$ and $\boldsymbol{a}_{\text{T}}(\cdot)$ denote the steering vectors of the receiver and transmitter antenna arrays, respectively, Δf denotes the subcarrier spacing, T_{mea} denotes transmission duration of each symbol, and ς denotes the wavelength. Each path i can be described by a complex gain g_k^i, a TOA τ_k^i, an AOA pair $\boldsymbol{\theta}_k^i$ in azimuth and elevation, an AOD pair $\boldsymbol{\phi}_k^i$ in azimuth and elevation, and a Doppler d_k^i which we express in [m/s]. These parameters can be estimated by a parametric channel estimation algorithm from $\boldsymbol{y}_{\kappa,n,k}$, for example, by [19]–[21], which is out of the scope of this paper, and the estimation results are utilized directly. Adding Doppler can make paths more resolvable, as there may be some paths not resolvable in delay or angle domains, but resolvable in the Doppler domain.

C. Measurement Model

At time step k, the channel estimator provides a set of measurements $\mathcal{Z}_k = \{\boldsymbol{z}_k^1, \ldots, \boldsymbol{z}_k^{\hat{I}_k}\}$, where usually $\hat{I}_k \neq I_k$, as some visible landmarks may be misdetected and there could be some clutter measurements. Please note that the source of each element in $\mathcal{Z}_k$ is unknown. If the measurement noise is zero-mean Gaussian, the measurement originating from landmark $\boldsymbol{x}^i$ at time step k can be described as follows

$$\boldsymbol{z}_k^i = \boldsymbol{h}(\boldsymbol{x}^i, \boldsymbol{s}_k) + \boldsymbol{\epsilon}_k^i, \tag{3}$$

where $\boldsymbol{h}(\boldsymbol{x}^i, \boldsymbol{s}_k) = [\tau_k^i, (\boldsymbol{\theta}_k^i)^{\mathsf{T}}, (\boldsymbol{\phi}_k^i)^{\mathsf{T}}, d_k^i]^{\mathsf{T}}$ represents the nonlinear function that transforms the geometric information to the channel parameters, and $\boldsymbol{\epsilon}_k \sim \mathcal{N}\left(\boldsymbol{0}, \boldsymbol{R}_k^i\right)$.

These channel parameters depend on the geometric relationships among the BS, the UE and the landmarks. Specifically, TOA τ_k^i can be defined as

$$\tau_k^i = \begin{cases} \|\boldsymbol{x}_{\text{BS}} - \boldsymbol{x}_{\text{UE},k}\|/c + b_k & m^i = \text{BS} \\ (\|\boldsymbol{x}_{\text{inc},k}^i - \boldsymbol{x}_{\text{UE},k}\| + \|\boldsymbol{x}_{\text{inc},k}^i - \boldsymbol{x}_{\text{BS}}\|)/c + b_k & m^i \neq \text{BS}, \end{cases} \tag{4}$$

where $\boldsymbol{x}_{\text{UE},k} = [x_k, y_k, 0]^{\mathsf{T}}$ denotes the 3D position of the UE, $\boldsymbol{x}_{\text{inc},k}^i$ is the incidence point of the i-th path on the corresponding landmark at time step k, which can be determined by $\boldsymbol{x}_{\text{LM}}^i$ and $\boldsymbol{x}_{\text{UE},k}$, and c is the speed of light. As $\boldsymbol{\theta}_k^i$ is determined by the arrival direction of the signal, which can be calculated by

$$\boldsymbol{q}^i_{\mathrm{AOA},k} = \begin{cases} (\boldsymbol{x}_{\mathrm{BS}} - \boldsymbol{x}_{\mathrm{UE},k})/\|\boldsymbol{x}_{\mathrm{BS}} - \boldsymbol{x}_{\mathrm{UE},k}\| & m^i = \mathrm{BS} \\ (\boldsymbol{x}^i_{\mathrm{inc},k} - \boldsymbol{x}_{\mathrm{UE},k})/\|\boldsymbol{x}^i_{\mathrm{inc},k} - \boldsymbol{x}_{\mathrm{UE},k}\| & m^i \neq \mathrm{BS}, \end{cases} \tag{5}$$

we can define $\boldsymbol{\theta}^i_k$ as

$$\theta^i_{\mathrm{az},k} = \mathrm{arctan2}([\boldsymbol{q}^i_{\mathrm{AOA},k}]_2, [\boldsymbol{q}^i_{\mathrm{AOA},k}]_1) - \varpi_k, \tag{6}$$

$$\theta^i_{\mathrm{el},k} = \arcsin([\boldsymbol{q}^i_{\mathrm{AOA},k}]_3, \|\boldsymbol{q}^i_{\mathrm{AOA},k}\|). \tag{7}$$

Similarly, the departure direction can be calculated by

$$\boldsymbol{q}^i_{\mathrm{AOD},k} = \begin{cases} (\boldsymbol{x}_{\mathrm{UE},k} - \boldsymbol{x}_{\mathrm{BS}})/\|(\boldsymbol{x}_{\mathrm{UE},k} - \boldsymbol{x}_{\mathrm{BS}})\| & m^i = \mathrm{BS} \\ (\boldsymbol{x}^i_{\mathrm{inc},k} - \boldsymbol{x}_{\mathrm{BS}})/\|\boldsymbol{x}^i_{\mathrm{inc},k} - \boldsymbol{x}_{\mathrm{BS}}\| & m^i \neq \mathrm{BS}, \end{cases} \tag{8}$$

and $\boldsymbol{\phi}^i_k$ can be defined as

$$\phi^i_{\mathrm{az},k} = \mathrm{arctan2}([\boldsymbol{q}^i_{\mathrm{AOD},k}]_2, [\boldsymbol{q}^i_{\mathrm{AOD},k}]_1), \tag{9}$$

$$\phi^i_{\mathrm{el},k} = \arcsin([\boldsymbol{q}^i_{\mathrm{AOD},k}]_3, \|\boldsymbol{q}^i_{\mathrm{AOD},k}\|). \tag{10}$$

The Doppler d^i_k can be calculated by projecting the UE velocity on the direction of $\boldsymbol{q}^i_{\mathrm{AOA},k}$, as displayed in Fig. 1. It can be computed by

$$d^i_k = \boldsymbol{v}^\mathsf{T}_k \boldsymbol{q}^i_{\mathrm{AOA},k}, \tag{11}$$

where $\boldsymbol{v}_k$ denotes the 3D velocity of the UE at time k, which can be defined as

$$\boldsymbol{v}_k = [v\cos\varpi_k, v\sin\varpi_k, 0]^\mathsf{T}, \tag{12}$$

since we assume the UE only moves on the $x-y$ plane. Therefore, d^i_k is positive, when the UE approaches the i-th landmark, and it is negative, when the UE moves away from the i-th landmark.

III. PROPOSED DOPPLER-ASSISTED SLAM

In this section, the PCRB is briefly introduced, the PEB, HEB, CEB and LEB are derived, and the contribution of Doppler to the SLAM system is analyzed.

A. PCRB

The PCRB is the lower bound that is analogous to the Cramér-Rao bound (CRB) but takes a Bayesian perspective and assumes that there is a prior on the parameters, indicating that the mean squared error (MSE) of an estimator should always be larger than the inverse of the posterior information matrix (PIM) [22, Ch. 4.2]. Suppose $\boldsymbol{\alpha}$ denotes a vector of the measurements, $\boldsymbol{\beta}$ denotes an r-dimensional estimated random parameter, and $\boldsymbol{g}(\boldsymbol{\alpha})$ denotes an estimate of $\boldsymbol{\beta}$, which is a function of $\boldsymbol{\alpha}$. The PCRB on the estimation error has the form

$$\mathbb{E}[(\boldsymbol{g}(\boldsymbol{\alpha}) - \boldsymbol{\beta})(\boldsymbol{g}(\boldsymbol{\alpha}) - \boldsymbol{\beta})^\mathsf{T}] \geq \boldsymbol{J}^{-1}, \tag{13}$$

where $\boldsymbol{J}$ is the $r \times r$ PIM with elements

$$[\boldsymbol{J}]_{\mu,\nu} = \mathbb{E}[-\frac{\partial^2 \log f(\boldsymbol{\alpha}, \boldsymbol{\beta})}{\partial\beta_\mu \partial\beta_\nu}] \qquad \mu, \nu = 1, \cdots, r, \tag{14}$$

with $f(\boldsymbol{\alpha}, \boldsymbol{\beta})$ denoting the joint density. The inequality in (13) indicates that the MSE of an estimator is larger than $\boldsymbol{J}^{-1}$ in the positive semidefinite sense. The PIM is a counterpart to the Fisher information matrix (FIM) for the PCRB, and can be decomposed into two parts $\boldsymbol{J} = \boldsymbol{J}_{\mathrm{data}} + \boldsymbol{J}_{\mathrm{prior}}$, where $\boldsymbol{J}_{\mathrm{data}}$ is the standard FIM, which contains information obtained from the measurements, and $\boldsymbol{J}_{\mathrm{prior}}$ is the priori information matrix, which contains prior information. The elements are given by (for $\mu, \nu = 1, \cdots, r$)

$$[\boldsymbol{J}_{\mathrm{data}}]_{\mu,\nu} = \mathbb{E}[-\frac{\partial^2 \log f(\boldsymbol{\alpha}|\boldsymbol{\beta})}{\partial\beta_\mu \partial\beta_\nu}], \tag{15}$$

$$[\boldsymbol{J}_{\mathrm{prior}}]_{\mu,\nu} = \mathbb{E}[-\frac{\partial^2 \log f(\boldsymbol{\beta})}{\partial\beta_\mu \partial\beta_\nu}]. \tag{16}$$

B. Performance Bounds

To compute the error bounds for the considered problem, we need to construct a complete state of the system, denoted as $\breve{\boldsymbol{s}}_k = [(\boldsymbol{s}_k)^\mathsf{T}, (\boldsymbol{x}^1_{\mathrm{LM},k})^\mathsf{T}, \ldots, (\boldsymbol{x}^I_{\mathrm{LM},k})^\mathsf{T}]^\mathsf{T}$, the transition function of the complete state, denoted as $\breve{\boldsymbol{f}}(\breve{\boldsymbol{s}}_k) = [(\boldsymbol{f}(\boldsymbol{s}_k))^\mathsf{T}, (\boldsymbol{x}^1_{\mathrm{LM},k})^\mathsf{T}, \ldots, (\boldsymbol{x}^I_{\mathrm{LM},k})^\mathsf{T}]^\mathsf{T}$, and the measurement function of the complete state given the ground-truth DA, denoted as $\breve{\boldsymbol{h}}(\breve{\boldsymbol{s}}_k) = [(\bar{\boldsymbol{h}}(\boldsymbol{s}_k, \boldsymbol{x}^1_{\mathrm{LM},k})^\mathsf{T}, \ldots, (\bar{\boldsymbol{h}}(\boldsymbol{s}_k, \boldsymbol{x}^I_{\mathrm{LM},k})^\mathsf{T}]^\mathsf{T}$, with $\bar{\boldsymbol{h}}(\boldsymbol{s}_k, \boldsymbol{x}^i_{\mathrm{LM},k}) = \boldsymbol{0}_{d_{\boldsymbol{z}}\times 1}$ when the landmark is not detected, and $\bar{\boldsymbol{h}}(\boldsymbol{s}_k, \boldsymbol{x}^i_{\mathrm{LM},k})$ is the same as $\boldsymbol{h}(\boldsymbol{s}_k, \boldsymbol{x}^i_{\mathrm{LM},k})$ when the landmark is detected. Then, if the ground-truth DA is given, the PIM can be recursively updated by [23], [24]

$$\boldsymbol{J}_k = \underbrace{\breve{\boldsymbol{H}}^\mathsf{T}_k \breve{\boldsymbol{R}}^{-1}_k \breve{\boldsymbol{H}}_k}_{\boldsymbol{J}_{\mathrm{data},k}} + \underbrace{\left(\breve{\boldsymbol{Q}}_k + \breve{\boldsymbol{F}}_k \boldsymbol{J}^{-1}_{k-1} \breve{\boldsymbol{F}}^\mathsf{T}_k\right)^{-1}}_{\boldsymbol{J}_{\mathrm{prior},k}}. \tag{17}$$

Here $\breve{\boldsymbol{H}}_k$ and $\breve{\boldsymbol{F}}_k$ are the Jacobian matrices of $\breve{\boldsymbol{h}}(\breve{\boldsymbol{s}}_k)$ and $\breve{\boldsymbol{f}}(\breve{\boldsymbol{s}}_k)$ with respect to $\breve{\boldsymbol{s}}_k$, evaluated at the true state, and $\breve{\boldsymbol{Q}}_k = \mathrm{blkdiag}(\boldsymbol{Q}, \boldsymbol{0}_{3I\times 3I})$ and $\breve{\boldsymbol{R}}_k = \mathrm{blkdiag}(\boldsymbol{R}^1_k, \cdots, \boldsymbol{R}^I_k)$ denote the process and measurement noise covariances, respectively. Then, the PEB can be computed as $\mathrm{PEB}_k = \sqrt{[\boldsymbol{J}_k]^{-1}_{1,1} + [\boldsymbol{J}_k]^{-1}_{2,2}}$, the HEB can be computed as $\mathrm{HEB}_k = \sqrt{[\boldsymbol{J}_k]^{-1}_{3,3}}$, the CEB can be computed as $\mathrm{CEB}_k = \sqrt{[\boldsymbol{J}_k]^{-1}_{4,4}}$, and the LEB of i-th landmark can be computed as $\mathrm{LEB}^i_k = \sqrt{\sum_{\mu=3i+2}^{3i+4} [\boldsymbol{J}_k]^{-1}_{\mu,\mu}}$.

C. Contribution of Doppler

From (17), we can observe that the Doppler of the current measurements only contribute to $\boldsymbol{J}_{\mathrm{data},k}$, as Doppler-related components are only involved in $\breve{\boldsymbol{H}}_k$ and $\breve{\boldsymbol{R}}_k$. As $\breve{\boldsymbol{H}}_k$ is the Jacobian matrices of $\breve{\boldsymbol{h}}(\breve{\boldsymbol{s}}_k)$ with respect to $\breve{\boldsymbol{s}}_k$, it can be correspondingly decomposed into blocks

$$\breve{\boldsymbol{H}}_k = \left[\begin{array}{c:ccccc} \boldsymbol{A}^1_k & \boldsymbol{B}^1_k & \boldsymbol{0}_{6\times 3} & \cdots & \boldsymbol{0}_{6\times 3} \\ \boldsymbol{A}^2_k & \boldsymbol{0}_{6\times 3} & \boldsymbol{B}^2_k & \ddots & \boldsymbol{0}_{6\times 3} \\ \vdots & \vdots & \ddots & \ddots & \vdots \\ \boldsymbol{A}^I_k & \boldsymbol{0}_{6\times 3} & \cdots & \boldsymbol{0}_{6\times 3} & \boldsymbol{B}^I_k \end{array}\right]. \tag{18}$$

Here, $\boldsymbol{A}^i_k$ and $\boldsymbol{B}^i_k$ are the Jacobian matrices of $\bar{\boldsymbol{h}}(\boldsymbol{s}_k, \boldsymbol{x}^i_{\mathrm{LM}})$ with respect to $\boldsymbol{s}_k$ and $\boldsymbol{x}^i_{\mathrm{LM}}$, respectively, which are $\boldsymbol{0}_{6\times 4}$ and $\boldsymbol{0}_{6\times 3}$ when the i-th landmark is not detected, and are

$$\boldsymbol{A}^i_k = \left[\begin{array}{c} \tilde{\boldsymbol{A}}^i_k \\ \hdashline (\tilde{\boldsymbol{a}}^i_k)^\mathsf{T} \end{array}\right], \quad \boldsymbol{B}^i_k = \left[\begin{array}{c} \tilde{\boldsymbol{B}}^i_k \\ \hdashline (\tilde{\boldsymbol{b}}^i_k)^\mathsf{T} \end{array}\right], \tag{19}$$

when the landmark is detected, where $\tilde{\boldsymbol{A}}_k^i$ is the Jacobian of $[\tau_k^i, (\boldsymbol{\theta}_k^i)^\mathsf{T}, (\boldsymbol{\phi}_k^i)^\mathsf{T}]^\mathsf{T}$ with respect to $\boldsymbol{s}_k$, $\tilde{\boldsymbol{B}}_k^i$ is the Jacobian of $[\tau_k^i, (\boldsymbol{\theta}_k^i)^\mathsf{T}, (\boldsymbol{\phi}_k^i)^\mathsf{T}]^\mathsf{T}$ with respect to $\boldsymbol{x}_{\text{LM}}^i$, and

$$(\tilde{\boldsymbol{a}}_k^i)^\mathsf{T} = [\ \tfrac{\partial d_k^i}{\partial x_k} \quad \tfrac{\partial d_k^i}{\partial y_k} \quad \tfrac{\partial d_k^i}{\partial \varpi_k} \quad \tfrac{\partial d_k^i}{\partial b_k}\ ], \tag{20}$$

$$(\tilde{\boldsymbol{b}}_k^i)^\mathsf{T} = [\ \tfrac{\partial d_k^i}{\partial x_{\text{LM}}^i} \quad \tfrac{\partial d_k^i}{\partial y_{\text{LM}}^i} \quad \tfrac{\partial d_k^i}{\partial z_{\text{LM}}^i}\ ]. \tag{21}$$

Furthermore, we assume $\boldsymbol{R}_k^i = \text{diag}(\tilde{\boldsymbol{R}}_k^i, (\sigma_{\text{d},k}^i)^2)$. According to (17) and the inverse of a block matrix, $\boldsymbol{J}_{\text{data},k}$ is only non-zero in the diagonal block related to the UE state

$$\begin{aligned}[\boldsymbol{J}_{\text{data},k}]_{1:4,1:4} &= \sum_{i=1}^{I} (\boldsymbol{A}_k^i)^\mathsf{T} (\boldsymbol{R}_k^i)^{-1} \boldsymbol{A}_k^i \\ &= \sum_{i=1}^{I} \underbrace{(\tilde{\boldsymbol{A}}_k^i)^\mathsf{T} (\tilde{\boldsymbol{R}}_k^i)^{-1} \tilde{\boldsymbol{A}}_k^i}_{\text{non-Doppler related}} + \sum_{i=1}^{I} \underbrace{\tilde{\boldsymbol{a}}_k^i (\sigma_{\text{d},k}^i)^{-2} (\tilde{\boldsymbol{a}}_k^i)^\mathsf{T}}_{\text{Doppler related}},\end{aligned} \tag{22}$$

and the diagonal blocks related to each landmark

$$\begin{aligned}[\boldsymbol{J}_{\text{data},k}]_{3i+2:3i+4,3i+2:3i+4} &= (\boldsymbol{B}_k^i)^\mathsf{T} (\boldsymbol{R}_k^i)^{-1} \boldsymbol{B}_k^i \\ &= \underbrace{(\tilde{\boldsymbol{B}}_k^i)^\mathsf{T} (\tilde{\boldsymbol{R}}_k^i)^{-1} \tilde{\boldsymbol{B}}_k^i}_{\text{non-Doppler related}} + \underbrace{\tilde{\boldsymbol{b}}_k^i (\sigma_{\text{d},k}^i)^{-2} (\tilde{\boldsymbol{b}}_k^i)^\mathsf{T}}_{\text{Doppler related}}.\end{aligned} \tag{23}$$

Clearly, Doppler provides non-negative information to both UE and landmark states. Due to the block-diagonal structure of $\boldsymbol{J}_{\text{data},k}$, (22) and (23) can be interpreted as the equivalent FIMs of the UE and landmark states.

To gain further insights, we expand $\tilde{\boldsymbol{a}}_k^i$ and $\tilde{\boldsymbol{b}}_k^i$ as

$$\tilde{\boldsymbol{a}}_k^i = \Big[-\frac{\big([\boldsymbol{v}_k]_{1:2} - d_k^i [\boldsymbol{q}_{\text{AOA},k}^i]_{1:2}\big)^\mathsf{T}}{\|\boldsymbol{x}_{\text{inc},k}^i - \boldsymbol{x}_{\text{UE},k}\|}, \boldsymbol{v}_{\perp,k}^\mathsf{T} \boldsymbol{q}_{\text{AOA},k}^i, 0\Big]^\mathsf{T}, \tag{24}$$

$$\tilde{\boldsymbol{b}}_k^i = \frac{\partial \boldsymbol{x}_{\text{inc},k}^i}{\partial \boldsymbol{x}_{\text{LM}}^i} \frac{\boldsymbol{v}_k - d_k^i \boldsymbol{q}_{\text{AOA},k}^i}{\|\boldsymbol{x}_{\text{inc},k}^i - \boldsymbol{x}_{\text{UE},k}\|}, \tag{25}$$

where $\boldsymbol{v}_{\perp,k} = [-v \sin \varpi_k, v \cos \varpi_k, 0]^\mathsf{T}$ (i.e., $\boldsymbol{v}_{\perp,k}^\mathsf{T} \boldsymbol{v}_k = 0$). Then, the additive Doppler-related parts in (22) and (23) can be summarized as follows:

- *UE position:* as $\boldsymbol{v}_k - d_k^i \boldsymbol{q}_{\text{AOA},k}^i = \boldsymbol{v}_k - \boldsymbol{v}_k^\mathsf{T} \boldsymbol{q}_{\text{AOA},k}^i \boldsymbol{q}_{\text{AOA},k}^i$, the information brought by Doppler is along the direction of the velocity, when the velocity is orthogonal to a path's $\boldsymbol{q}_{\text{AOA},k}^i$ direction, i.e., when $\boldsymbol{v}_k^\mathsf{T} \boldsymbol{q}_{\text{AOA},k}^i = 0$. On the other hand, when the velocity is parallel to a path's $\boldsymbol{q}_{\text{AOA},k}^i$ direction, the Doppler of that path does not provide direct Fisher information. A similar argument holds for landmark locations.
- *Heading ϖ_k:* the direct contribution is from the projection of $\boldsymbol{v}_{\perp,k}$ on the direction of $\boldsymbol{q}_{\text{AOA},k}^i$ of each path. Hence, if the UE velocity is parallel to a path's $\boldsymbol{q}_{\text{AOA},k}^i$ direction, the direct Fisher information is 0.
- *Clock bias b_k:* there is no direct Fisher information contribution. However, the direct contributions to the other dimensions still benefit estimate of the clock bias.

Therefore, if the UE moves alongside the same or the opposite direction of the $\boldsymbol{q}_{\text{AOA},k}^i$, the corresponding group of measurement does not have any Doppler-related information. Moreover, a smaller $(\sigma_{\text{d},k}^i)^2$ results in larger additional Doppler-related information.

IV. EK-PMB(M) SLAM FILTER

The SLAM framework in this paper follows the EK-PMB SLAM filter proposed in [16]. In this section, the basics of the PMB(M) density and the EK-PMB(M) SLAM filter are summarized in the following.

A. Basics of PMB(M) Density

The map of the environment $\mathcal{X}$ is formulated as a PMBM RFS, which can be viewed as the union of two disjoint RFSs: $\mathcal{X}_\text{U}$ for the set of undetected landmarks, which are the landmarks that have never been detected, and $\mathcal{X}_\text{D}$ for the set of detected landmarks, which are the the landmarks that have been detected at least once before. Its density follows [25]

$$f(\mathcal{X}) = \sum_{\mathcal{X}_\text{U} \uplus \mathcal{X}_\text{D} = \mathcal{X}} f_\text{P}(\mathcal{X}_\text{U}) f_\text{MBM}(\mathcal{X}_\text{D}), \tag{26}$$

where $\mathcal{X}_\text{U}$ and $\mathcal{X}_\text{D}$ are modeled as a Poisson point process (PPP) and a multi-Bernoulli mixture (MBM), respectively, with densities following

$$f_\text{P}(\mathcal{X}_\text{U}) = e^{-\int \lambda(\boldsymbol{x}) \text{d}\boldsymbol{x}} \prod_{\boldsymbol{x} \in \mathcal{X}_\text{U}} \lambda(\boldsymbol{x}), \tag{27}$$

$$f_\text{MBM}(\mathcal{X}_\text{D}) \propto \sum_{j \in \mathbb{I}} w^j \sum_{\mathcal{X}^1 \uplus \cdots \uplus \mathcal{X}^{|\mathcal{X}_\text{D}|} = \mathcal{X}_\text{D}} \prod_{i=1}^{|\mathcal{X}_\text{D}|} f_\text{B}^{j,i}(\mathcal{X}^i). \tag{28}$$

Here, $\lambda(\cdot)$ denotes the intensity function of the PPP density, and $\mathbb{I}$ is the index set of all global hypotheses with weights satisfying $\sum_{j \in \mathbb{I}} w^j = 1, w^j \geq 0$, and the global hypotheses in SLAM correspond to different DAs [26]. Each individual component in (28) is termed as a Bernoulli process, and $f_\text{B}^{j,i}(\cdot)$ denotes the Bernoulli density of the i-th landmark under the j-th global hypothesis, following

$$f_\text{B}^{j,i}(\mathcal{X}^i) = \begin{cases} 1 - r^{j,i} & \mathcal{X}^i = \emptyset \\ r^{j,i} f^{j,i}(\boldsymbol{x}) & \mathcal{X}^i = \{\boldsymbol{x}\} \\ 0 & \text{otherwise}, \end{cases} \tag{29}$$

where $f^{j,i}(\cdot)$ denotes the state density, and $r^{j,i} \in [0,1]$ denotes the probability that the corresponding landmark exists. We note that if there is only one mixture component in the MBM, then (28) reduces to a multi-Bernoulli (MB), and (26) reduces to a PMB.

B. EK-PMB(M) SLAM Filter Recursion

The EK-PMB(M) SLAM filter follows the Bayesian filtering recursion with RFSs, and it computes the joint posterior $f(\boldsymbol{s}_{k+1}, \mathcal{X} | \mathcal{Z}_{1:k+1})$ by [16]

$$\begin{aligned} f(\boldsymbol{s}_{k+1}, \mathcal{X} | \mathcal{Z}_{1:k+1}) \propto\ & \ell(\mathcal{Z}_{k+1} | \boldsymbol{s}_{k+1}, \mathcal{X}) f(\mathcal{X} | \mathcal{Z}_{1:k}) \\ & \times f(\boldsymbol{s}_{k+1} | \mathcal{Z}_{1:k}), \end{aligned} \tag{30}$$

with $f(\boldsymbol{s}_{k+1} | \mathcal{Z}_{1:k}) = \int f(\boldsymbol{s}_k | \mathcal{Z}_{1:k}) f(\boldsymbol{s}_{k+1} | \boldsymbol{s}_k) \text{d}\boldsymbol{s}_k$ and $\ell(\mathcal{Z}_{k+1} | \boldsymbol{s}_{k+1}, \mathcal{X})$ denoting the RFS likelihood function, given by [25, eqs. (5)–(6)]. Instead of tracking the joint density, the filter keeps track of the marginal UE $f(\boldsymbol{s}_k | \mathcal{Z}_{1:k})$ and map

$f(\mathcal{X}|\mathcal{Z}_{1:k})$ posteriors by marginalizing out the map and the UE state from the joint posterior, respectively. The marginal posteriors are given by

$$f(\boldsymbol{s}_{k+1}|\mathcal{Z}_{1:k+1}) = \int f(\boldsymbol{s}_{k+1}, \mathcal{X}|\mathcal{Z}_{1:k+1})\delta\mathcal{X}, \tag{31}$$

$$f(\mathcal{X}|\mathcal{Z}_{1:k+1}) = \int f(\boldsymbol{s}_{k+1}, \mathcal{X}|\mathcal{Z}_{1:k+1})\mathrm{d}\boldsymbol{s}_{k+1}, \tag{32}$$

where $\int \psi(\mathcal{X})\delta\mathcal{X}$ refers to the set integral [26, eq. (4)].

The EK-PMB(M) SLAM filter proposed in [16] determines $\gamma \geq 1$ most likely DAs for each prior global hypothesis with corresponding weights, and the joint posterior of the UE state and the map conditioned on each DA is computed by utilizing an extended Kalman filter (EKF)-like update step. Then the joint posterior in (30) can be acquired by the weighted summation of the densities for DAs, followed by (31) and (32) to compute the UE state and the map. To avoid the exponential increase of DAs, we can approximate the PMBM density to a PMB density at the end of each update step, which reduces the complexity significantly.

It is important to mention that the weights of $\gamma \geq 1$ most likely DAs for each prior global hypothesis are computed by using measurements [16, eq. (29)]. Since more information is provided with the involvement of Doppler, finding the correct DAs becomes more likely, as correct local hypothesis weights computed in [16, eqs. (22)–(24)] become more prominent.

V. RESULTS

A. Simulation Environment

We consider a 5G downlink scenario with a single BS located at $[0\,\mathrm{m}, 0\,\mathrm{m}, 40\,\mathrm{m}]^\mathsf{T}$, 4 VAs located at $[\pm 200\,\mathrm{m}, 0\,\mathrm{m}, 40\,\mathrm{m}]^\mathsf{T}$, $[0\,\mathrm{m}, \pm 200\,\mathrm{m}, 40\,\mathrm{m}]^\mathsf{T}$, and 4 SPs located at $[\pm 99\,\mathrm{m}, 0\,\mathrm{m}, 10\,\mathrm{m}]^\mathsf{T}$, $[0\,\mathrm{m}, \pm 99\,\mathrm{m}, 10\,\mathrm{m}]^\mathsf{T}$. The UE does a counterclockwise constant turn-rate movement around the BS according to (1), with $v = 22.22$ m/s, $\omega = \pi/10$ rad/s, $T = 0.5$ s, and $\mathbf{Q} = \mathrm{diag}(0.2^2\ \mathrm{m}^2, 0.2^2\ \mathrm{m}^2, 0.001^2\ \mathrm{rad}^2, 0.2^2\ \mathrm{m}^2)$, and it takes $K = 40$ samples for the UE to circle the road once. The measurement covariance matrix is set as $\boldsymbol{R}_k^i = \mathrm{blkdiag}(10^{-2}\ \mathrm{m}^2, 2.5 \times 10^{-3} \cdot \mathbf{I}_4\ \mathrm{rad}^2, \sigma_\mathsf{d}^2)$. We initialize the UE at $[70.7285\,\mathrm{m}, 0\,\mathrm{m}, \pi/2\,\mathrm{rad}, 300\,\mathrm{m}]^\mathsf{T}$ with covariance as $\mathrm{diag}[0.3\,\mathrm{m}^2, 0.3\,\mathrm{m}^2\ 0.0052\,\mathrm{rad}^2, 0.3\,\mathrm{m}^2]$. The BS is a priori known to the UE. We implemented the EK-PMB SLAM filter with considering $\gamma = 10$ best DAs every time step, and compared the results of cases using different levels of σ_d and without considering Doppler. The mapping performance is quantified by the generalized optimal subpattern assignment (GOSPA) distance [27] for both VAs and SPs, separately, the positioning performance is evaluated by the root mean squared error (RMSE), and we also compare bounds of different cases. More details on parametric settings of the filter can be found in [16]. The results are averaged over 100 Monte Carlo simulations.

B. Results and Discussion

We firstly analyze how different levels of σ_d affect the bounds. Fig. 2 shows how the bounds change with σ_d, compared with the bounds without considering Doppler. We observe that involving Doppler as a dimension of the measurement improves the positioning and mapping performances of the SLAM system, as the error bounds are lower than in the case where the Doppler measurement is ignored. This effect is stronger when Doppler measurements are more accurate, i.e., when σ_d is smaller.

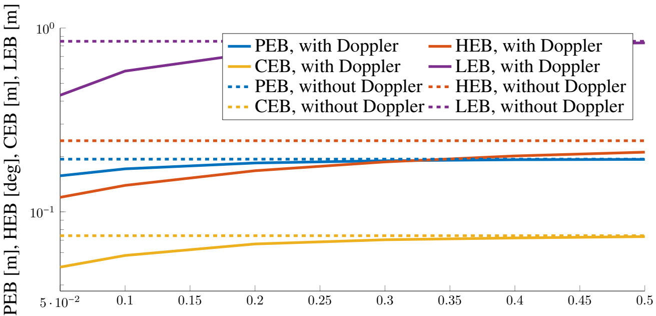

Fig. 2. The PEB, the HEB, the CEB and the average LEB change with σ_d. The benchmarks are the bounds of the case without considering Doppler.

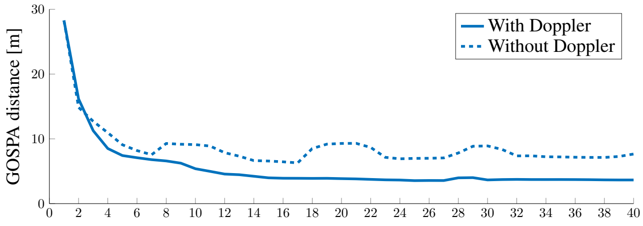

Fig. 3. Comparison of mapping performances for VAs between two cases: with and without considering Doppler.

To validate the benefits of Doppler in mmWave radio SLAM, we then implement the EK-PMB SLAM filter on two cases: 1) involving Doppler into the measurement with $\sigma_\mathsf{d} = 0.1$ m/s and 2) without considering Doppler, and compare the mapping performance for both VAs and SPs, and the positioning performance between two cases, as illustrated in Fig. 3, Fig. 4 and Fig. 5, respectively. Fig. 3 and Fig. 4 demonstrate that the SLAM filter can map the environment for both cases, and the mapping accuracy improves with more measurements being received, as overall, all GOSPA distances gradually decrease over time. Clearly, when Doppler is involved, the SLAM filter has better mapping performance, as the solid lines are lower than the dashed lines in both Fig. 3 and Fig. 4. Fig. 5 indicates that considering Doppler results in better UE state estimates, as lower RMSEs can be acquired. The reasons are that considering Doppler as a dimension of the measurement brings lower bounds. In addition, it also helps the SLAM filter to solve the DA problem, which improves the average weight for the correct DA from 0.6763 to 0.8622, with weights of all selected $\gamma = 10$ DAs summed to 1 every time step.

VI. CONCLUSIONS

In this paper, we exploited Doppler as a part of measurement in bistatic mmWave radio SLAM, formulated the EK-PMB SLAM filter on the new measurement model, and provided the PCRB for the model. Our results theoretically

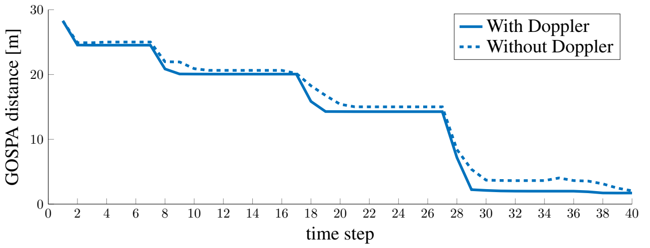

Fig. 4. Comparison of mapping performances for SPs between two cases: with and without considering Doppler.

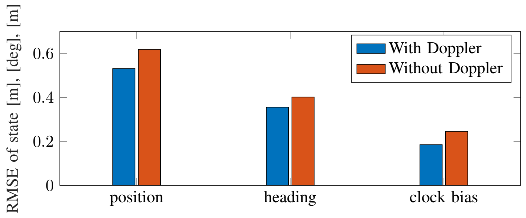

Fig. 5. Comparison of UE state estimation between two cases: with and without considering Doppler.

indicate that the involvement of Doppler helps the SLAM filter to acquire better mapping and positioning performance than the case without considering Doppler. The better Doppler observations are, the lower PCRBs and the more accurate map and UE state estimates will be. The implementation of the EK-PMB SLAM filter validates the theoretical benefits of involving Doppler. Future work will include extending the UE model to a model with unknown speed, the inclusion of high-dimensional channel estimation, as well as extending the SLAM problem to a simultaneous localization and tracking (SLAT) problem.

ACKNOWLEDGMENT

This work was partially supported by the Wallenberg AI, Autonomous Systems and Software Program (WASP) funded by Knut and Alice Wallenberg Foundation, and the Vinnova 5GPOS project under grant 2019-03085, by the Swedish Research Council under grant 2018-03705, and by the Academy of Finland under the grants #315858, #328214, #319994, #323244, #346622.

REFERENCES

[1] J. Nurmi, E.-S. Lohan, H. Wymeersch, G. Seco-Granados, and O. Nykänen, *Multi-Technology Positioning*. Springer, 2017.

[2] N. Patwari, J. Ash, S. Kyperountas, A. Hero, R. Moses, and N. Correal, "Locating the nodes: cooperative localization in wireless sensor networks," *IEEE Signal Processing Magazine*, vol. 22, no. 4, pp. 54–69, 2005.

[3] M. D. Larsen, A. L. Swindlehurst, and T. Svantesson, "Performance bounds for MIMO-OFDM channel estimation," *IEEE Transactions on Signal Processing*, vol. 57, no. 5, pp. 1901–1916, 2009.

[4] H. Wymeersch, G. Seco-Granados, G. Destino, D. Dardari, and F. Tufvesson, "5G mmWave positioning for vehicular networks," *IEEE Wireless Communications*, vol. 24, no. 6, pp. 80–86, 2017.

[5] S. M. Patole, M. Torlak, D. Wang, and M. Ali, "Automotive radars: A review of signal processing techniques," *IEEE Signal Processing Magazine*, vol. 34, no. 2, pp. 22–35, 2017.

[6] A. Amar and A. J. Weiss, "Localization of narrowband radio emitters based on doppler frequency shifts," *IEEE Transactions on Signal Processing*, vol. 56, no. 11, pp. 5500–5508, 2008.

[7] Y. Han, Y. Shen, X.-P. Zhang, M. Z. Win, and H. Meng, "Performance limits and geometric properties of array localization," *IEEE Transactions on Information Theory*, vol. 62, no. 2, pp. 1054–1075, 2016.

[8] A. Kakkavas, M. H. C. García, R. A. Stirling-Gallacher, and J. A. Nossek, "Performance limits of single-anchor millimeter-wave positioning," *IEEE Trans. Wireless Commun.*, vol. 18, no. 11, pp. 5196–5210, Aug. 2019.

[9] K. Qian, C. Wu, Z. Yang, Y. Liu, and K. Jamieson, "Widar: Decimeter-level passive tracking via velocity monitoring with commodity Wi-Fi," in *Proceedings of the 18th ACM International Symposium on Mobile Ad Hoc Networking and Computing*, 2017.

[10] F. Wen, J. Kulmer, K. Witrisal, and H. Wymeersch, "5G positioning and mapping with diffuse multipath," *IEEE Transactions on Wireless Communications*, vol. 20, no. 2, pp. 1164–1174, 2020.

[11] A. Yassin, Y. Nasser, A. Y. Al-Dubai, and M. Awad, "MOSAIC: Simultaneous localization and environment mapping using mmwave without a-priori knowledge," *IEEE Access*, vol. 6, pp. 68 932–68 947, 2018.

[12] E. Leitinger, F. Meyer, F. Hlawatsch, K. Witrisal, F. Tufvesson, and M. Z. Win, "A belief propagation algorithm for multipath-based SLAM," *IEEE Trans. Wireless Commun.*, vol. 18, no. 12, pp. 5613–5629, Sep. 2019.

[13] R. Mendrzik, F. Meyer, G. Bauch, and M. Z. Win, "Enabling situational awareness in millimeter wave massive MIMO systems," *IEEE J. Sel. Topics Signal Process.*, vol. 13, no. 5, pp. 1196–1211, Aug. 2019.

[14] H. Kim, K. Granström, L. Gao, G. Battistelli, S. Kim, and H. Wymeersch, "5G mmWave cooperative positioning and mapping using multi-model PHD filter and map fusion," *IEEE Transactions on Wireless Communications*, 2020.

[15] Y. Ge, F. Wen, H. Kim, M. Zhu, F. Jiang, S. Kim, L. Svensson, and H. Wymeersch, "5G SLAM using the clustering and assignment approach with diffuse multipath," *Sensors (Basel, Switzerland)*, vol. 20, no. 16, August 2020. [Online]. Available: https://doi.org/10.3390/s20164656

[16] Y. Ge, O. Kaltiokallio, H. Kim, F. Jiang, J. Talvitie, M. Valkama, L. Svensson, S. Kim, and H. Wymeersch, "A computationally efficient EK-PMBM filter for bistatic mmWave radio SLAM," *IEEE Journal on Selected Areas in Communications*, 2022.

[17] M. Roth, G. Hendeby, and F. Gustafsson, "EKF/UKF maneuvering target tracking using coordinated turn models with polar/cartesian velocity," in *17th International Conference on Information Fusion*, 2014, pp. 1–8.

[18] R. W. Heath, N. Gonzalez-Prelcic, S. Rangan, W. Roh, and A. M. Sayeed, "An overview of signal processing techniques for millimeter wave MIMO systems," *IEEE Journal of Selected Topics in Signal Processing*, vol. 10, no. 3, pp. 436–453, 2016.

[19] A. Richter, "Estimation of radio channel parameters: Models and algorithms," Ph.D. dissertation, Ilmenau University of Technology, 2005.

[20] A. Alkhateeb, O. El Ayach, G. Leus, and R. W. Heath, "Channel estimation and hybrid precoding for millimeter wave cellular systems," *IEEE Journal of Selected Topics in Signal Processing*, vol. 8, no. 5, pp. 831–846, 2014.

[21] F. Jiang, Y. Ge, M. Zhu, and H. Wymeersch, "High-dimensional channel estimation for simultaneous localization and communications," in *IEEE Wireless Communications and Networking Conference (WCNC)*, 2021.

[22] H. L. Van Trees, *Detection, Estimation, and Dodulation Theory, Part I: Detection, Estimation, and Linear Modulation Theory*. John Wiley & Sons, 2004.

[23] P. Tichavsky, C. H. Muravchik, and A. Nehorai, "Posterior Cramér-Rao bounds for discrete-time nonlinear filtering," *IEEE Transactions on Signal Processing*, vol. 46, no. 5, pp. 1386–1396, 1998.

[24] O. Kaltiokallio, Y. Ge, J. Talvitie, H. Wymeersch, and M. Valkama, "mmWave simultaneous localization and mapping using a computationally efficient EK-PHD filter," in *IEEE International Conference on Information Fusion (Fusion)*, 2021.

[25] Á. F. García-Fernández, J. L. Williams, K. Granström, and L. Svensson, "Poisson multi-Bernoulli mixture filter: Direct derivation and implementation," *IEEE Transactions on Aerospace and Electronic Systems*, vol. 54, no. 4, pp. 1883–1901, 2018.

[26] J. L. Williams, "Marginal multi-Bernoulli filters: RFS derivation of MHT, JIPDA, and association-based MeMBer," *IEEE Transactions on Aerospace and Electronic Systems*, vol. 51, no. 3, pp. 1664–1687, 2015.

[27] A. S. Rahmathullah, Á. F. García-Fernández, and L. Svensson, "Generalized optimal sub-pattern assignment metric," in *20th IEEE International Conference on Information Fusion (Fusion)*, 2017.